PAPER

Check for updates

LiSi₃As₆ and Li₂SiAs₂ with flexible SiAs₂ polyanions: synthesis, structure, bonding, and ionic conductivity†

$LiSi_3As_6$ and Li_2SiAs_2 with flexible $SiAs_2$ polyanions: synthesis, structure, bonding, and ionic conductivity†

Justin Mark, [ID] [ab] Kathleen Lee,‡[c] Maxwell A. T. Marple,[d] Shannon Lee, [ID] [ab] Sabyasachi Sen[d] and Kirill Kovnir [ID] ⋆[ab]

Two novel ternary phases, $LiSi_3As_6$ and Li_2SiAs_2, have been synthesized and characterized. Both phases have an identical Si : As ratio of 1 : 2 providing insight on how layers of the parent phase $SiAs_2$ accommodate excess electrons from Li cations to form Si–As anionic frameworks. $LiSi_3As_6$ exhibits a variety of bonding schemes involving Si–Si and As–As bonds, as well as corner-sharing $SiAs_4$ tetrahedra, while Li_2SiAs_2 is isostructural to the previously reported Li_2SiP_2, with adamantane-like Si_4As_{10} units connected into 3D framework. $LiSi_3As_6$ and Li_2SiAs_2 are predicted to be indirect semiconductors which was experimentally confirmed by optical properties characterization. Li_2SiAs_2 exhibits low thermal conductivity of 1.20 W m⁻¹ K⁻¹ at 300 K in combination with a room temperature ionic conductivity of 7×10^{-6} S cm⁻¹, an order of magnitude greater than that of the phosphide and nitride analogues, indicating its potential as a solid-state Li-ion conductor.

Introduction

Ionic conductivity is one of the fundamental properties of matter which is highly demanded for various applications from membranes and sensors to fuel cells and batteries. Discovery of novel compounds containing the desired ions and understanding of basic structure–properties relationships is crucial for the development of novel ion conductors. For example, in batteries, oxide and nitride materials were traditionally considered as potential Li and Na solid ion conductors, such as NASICON, LISICON, garnet, and perovskite type conductors.[1–5] Recent discovery of the novel crystalline phase $Li_{10}GeP_2S_{12}$ with extraordinary ionic conductivity pointed out the potential of non-oxide systems.[6–13] Indeed, a reduction of the ionicity of the Li–X bonds (where Li is surrounded by X atoms) should result in easier Li transport, as shown through comparing oxides vs. phosphides.[14] This pointed to the necessity to study complex Li

pnictides, which led to the recent discovery of several promising Li–Si–P phases, such as $Li_{14}SiP_6$, $Li_{10}Si_2P_6$, Li_8SiP_4, $Li_3Si_3P_7$, Li_2SiP_2, and $LiSi_2P_3$.[15–18] These recent works revealed that the Li–Si–P system was poorly investigated with the only previously reported compound, Li_5SiP_3, having been identified in 1954.[19] In the same article by Juza and Schulz, the first Li–Si–As compound Li_5SiAs_3 was also reported.[19]

Given the many similarities in phosphide and arsenide chemistry, we explored the Li–Si–As system for new phases to investigate further reduction of the ionicity of Li–X bonds and changes in Li conductivity. Upon our exploration of Li intercalation into the binary layered SiAs we reported a novel layered compound, $Li_3Si_7As_8$, which was only the second phase ever reported in this ternary phase space.[20] Based on the existence of another binary silicon arsenide, $SiAs_2$, we kept the Si : As ratio as 1 : 2 and studied how the Si–As anionic framework would react to different concentrations of Li cations (Fig. 1). This has resulted in the discovery of two new phases, $LiSi_3As_6$ ($=Li_{0.33}SiAs_2$) and Li_2SiAs_2, with the latter being isostructural to previously reported Li_2SiP_2.[17,18] $LiSi_3As_6$ exhibits an intricate structure and bonding demonstrating that the complex bonding motifs frequently exhibited by silicon-phosphides are also available to the arsenide counterparts. Si–As frameworks in both reported crystal structures differ from that in the Li-free $SiAs_2$ due to the extra electrons provided by Li cations causing Si–As bonding rearrangements. In this work we report on the syntheses and crystal structures of the title phases and detailed characterization of heat transport properties and Li-conductivity of Li_2SiAs_2.

[a]Department of Chemistry, Iowa State University, Ames, Iowa 50011, USA. E-mail: kovnir@iastate.edu

[b]Ames Laboratory, U.S. Department of Energy, Ames, Iowa 50011, USA

[c]Department of Chemistry, University of California, Davis, Davis, CA 95616, USA

[d]Department of Materials Science and Engineering, University of California, Davis, Davis, CA 95616, USA

3322 | J. Mater. Chem. A, 2020, 8, 3322–3332

This journal is © The Royal Society of Chemistry 2020

Experimental

Warning

At high temperatures the As vapor pressure may be sufficient to damage the reaction ampoule. Another possible reason for ampoule failure is the reaction of silica with Li. In either case, the release of toxic As vapor will occur. The concentration of As should be kept to a minimum. Use of the secondary larger size ampoule and placing the furnace in a well-ventilated space like a fumehood is highly recommended.

Synthesis

All materials were handled in an Ar-filled glovebox with O_2 levels < 1 ppm. The starting materials, Si (Alfa Aesar, 99.999%) and gray As (Alfa Aesar, 99.9999%) were used as received. The surface of the Li granules (Alfa Aesar, 99%) was scraped off to remove any surface oxidation.

A single crystal of $LiSi_3As_6$ was first obtained by loading elemental Li, Si, and As into a carbonized silica ampoule (9/11 mm inner/outer diameter) in a 0.8 : 3 : 3 ratio, respectively. The ampoule was then flame sealed under vacuum. The initial ampoule was then placed into a larger silica ampoule and flame sealed under vacuum to create a protective outer jacket. The ampoule was placed in a muffle furnace and heated to 923 K over 48 h. The sample was annealed at this temperature for 240 h and then slowly cooled to room temperature over 48 h. It was subsequently found that $LiSi_3As_6$ could be synthesized by a stoichiometric mixture of the elements, under the same conditions, however the sample was still contaminated with significant amounts of $SiAs_2$, Si, and As admixtures. Reducing the reaction temperature to 823 K prevents $SiAs_2$ formation, however unreacted Si and As remain. Further attempts to synthesize single phase samples by varying the temperature profile were unsuccessful.

Li_2SiAs_2 was first synthesized by loading elemental Li, Si, and As in a 0.5 : 1 : 2 ratio into a Nb ampoule, which resulted in

a mixture of Li_2SiAs_2 as well as SiAs, Si, and As. Single phase samples of Li_2SiAs_2 were prepared using a stoichiometric ratio of the elements sealed in a Nb ampoule under Ar atmosphere. The Nb ampoule was then sealed inside a silica ampoule under vacuum to prevent Nb oxidation during annealing. The ampoule was placed in a muffle furnace and heated to 523 K over 24 h, annealed at this temperature for 24 h, and heated to 923 K over 24 h, and annealed at this temperature for 96 h. The furnace was then turned off and the furnace was cooled to room temperature. The product is a red powder that degrades after several minutes of exposure to ambient conditions.

X-ray diffraction

Powder X-ray diffraction (XRD) was performed using a Rigaku Miniflex 600 with Cu-K_α radiation and a Ni-K_β filter using sample holders with a zero-background silicon plate insert (Fig. 2).

Single crystal XRD was performed using a Bruker AXS SMART diffractometer and Bruker D8 Venture diffractometer, both utilizing Mo-K_α radiation. Datasets were collected at 90 K under a N_2 stream and under ambient conditions with ω-scans
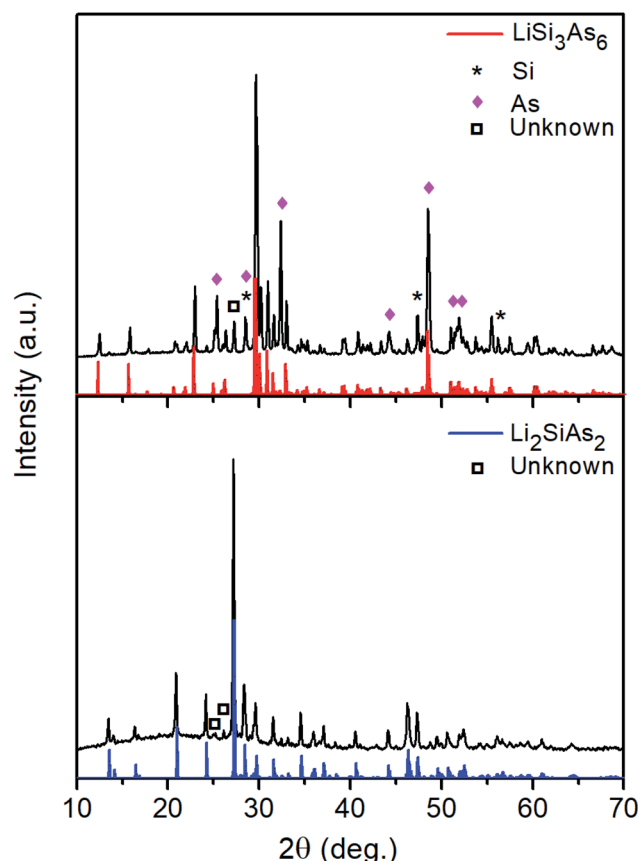

Fig. 2 Powder X-ray diffraction patterns of as-synthesized $LiSi_3As_6$ (top) and Li_2SiAs_2 (bottom). Below each experimental pattern (black) is a calculated pattern based on the crystal structure for $LiSi_3As_6$ (red) and Li_2SiAs_2 (blue). The admixture peaks are indicated in the legend. While $LiSi_3As_6$ is not single phase, the Li_2SiAs_2 contain minimum amounts of admixture which may also be generated during XRD experiment due to exposure to air.
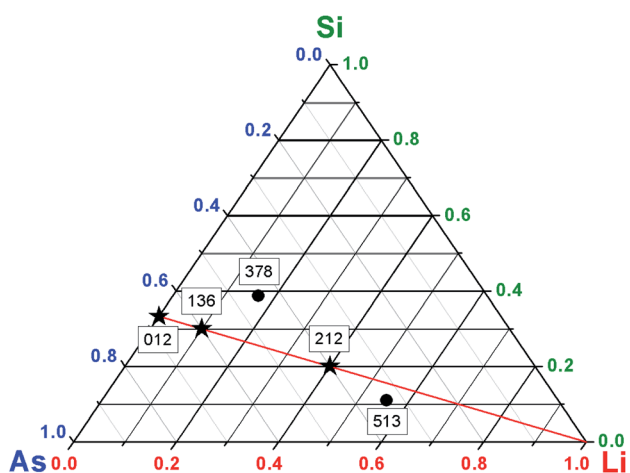

Fig. 1 Ternary phase diagram for the Li–Si–As system. $SiAs_2$, $LiSi_3As_6$, and Li_2SiAs_2 are shown as stars connected with a red line, while Li_5SiAs_3 and $Li_3Si_7As_8$ are shown as circles.[19,20] The labels of the compounds correspond to the stoichiometric ratios of Li : Si : As.

recorded with a 0.3° step width and integrated with the Bruker SAINT software. Structure determination and refinement of the crystal structures were carried out using the SHELX suite of programs.[21] Further details of the crystal structure determination may be found through Cambridge Crystallographic Data Centre by using CCDC-1954349 (Li_2SiAs_2) and CCDC-1954350 ($LiSi_3As_6$).†

Scanning electron microscopy energy-dispersive X-ray spectroscopy (SEM-EDXS)

Elemental analyses of selected crystals of for $LiSi_3As_6$ were performed using a FEI Quanta 250 field emission-SEM with EDXS detection (Oxford X-Max 80) and Aztec software (Fig. S3†). Samples were mounted in epoxy, polished to a level surface, coated with a conductive layer of carbon, and then mounted onto carbon tape. The average Si : As ratio was determined to be 1 : 2.1(4) based on scans of 12 sites, confirming the 1 : 2 Si : As ratio for $LiSi_3As_6$.

Diffuse reflectance spectroscopy

UV-vis diffuse reflectance spectrum of Li_2SiAs_2 was recorded using a Thermo Scientific Evolution 220 Spectrometer equipped with an integrating sphere. The reflectance data were converted to the Kubelka–Munk function, $f(R) = (1 - R)^2(2R)^{-1}$. Samples were cold-pressed into an 8 mm diameter pellet in an Ar-filled glovebox. The pellet was sealed inside a polypropylene bag to ensure the sample would not oxidize during the measurement. An empty polypropylene bag was used for the background scans.

Differential scanning calorimetry (DSC)

Differential scanning calorimetry was performed on a Netzcsh STA 449 F3 Jupiter and Netzsch DSC 404 F3 Pegasus Differential Scanning Calorimeters. Approximately 30–50 mg of sample were sealed inside evacuated silica ampoules. $LiSi_3As_6$ was heated at a rate of 10 K min^{-1} with a max temperature of 1073 K and cooled to room temperature at the same rate. Li_2SiAs_2 was heated to 1273 K and cooled to room temperature at a rate of 10 K min^{-1}. XRD patterns were collected after DSC experiments (Fig. S2†).

Quantum chemical calculations

Electronic structure calculations including the band structure, density of states (DOS), and electron localization function (ELF) analyses, were carried out using the tight-binding linear muffin-tin orbital atomic sphere approximation (TB-LMTO-ASA) package.[22] The Barth Hedin exchange potential was used for the LDA calculations.[23] A basis set of As(4s, 4p), Si(3s, 3p), and Li(2s) orbitals was used with downfolded As(4d), Si(3d), Li(2p, 3d) orbitals. The DOS and band structures for $LiSi_3As_6$ were calculated after converging the total energy on a k-mesh of $8 \times 8 \times 8$ points with 105 irreducible k-points, while Li_2SiAs_2 was computed with a k-mesh of $8 \times 8 \times 8$ points with 59 irreducible k-points. The ELF (η)[24–27] was evaluated with modules

implemented within the TB-LMTO-ASA program package. The ParaView program was used for visualization of ELF.[28,29]

Spark plasma sintering (SPS)

All manipulation and handling of Li_2SiAs_2 samples and SPS dies were performed in an Ar-filled glovebox. Finely ground powder was loaded into a 5 mm diameter graphite die between two sheets of graphite foil and WC plungers. This assembly was loaded into a protective outer graphite die with graphite plungers. The sample was quickly transferred to the SPS (Dr Sinter Lab Jr SPS-211Lx, Sumitomo Coal Mining Co., Ltd.) to limit the exposure to air. A uniaxial pressure of 50 MPa was applied while the sample was heated to 648 K over 4 minutes, then heated to 748 K over 5 minutes. The sample was annealed at this temperature for 10 minutes while the pressure was increased to 127 MPa. The pressure was then released, and the sample was cooled to room temperature. The assembly was quickly transferred to an Ar-filled glovebox where the surfaces were polished to remove any traces of graphite.

Li-conductivity

Electrical conductivity was measured by ac impedance methods using a HP 4192A impedance analyzer with a frequency range of 30 Hz to 13 MHz (Fig. S4 and S5†). Colloidal silver paste (Ted Pella) was applied to pellets sintered *via* SPS and cured to form the electrodes. The sample was measured within an Ar filled glovebox through a temperature range of 300–369 K. Measurements were carried out after the sample's temperature reached equilibrium. ZView software was used to analyze the impedance spectra through simulation with a series of parallel resistor and constant phase elements for bulk and grain boundary responses.
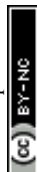
Determination of the ionic transference number was accomplished by using the dc polarization technique on a cell of Ag/Li_2SiAs_2/Li. A Keithley 230 voltage source in series with a Keithley 617 electrometer was used to simultaneously apply 5 mV and measure the current response with time. The polarity of the cell (+)Ag/Li_2SiAs_2/Li(−) results in depletion of Li ions at the Ag electrode/Li_2SiAs_2 interface allowing only electronic charge carriers as the source of electrical current. Comparing the initial current when the voltage was activated to the current after reaching steady state provides the electronic contribution to conductivity and consequently the ionic transference number through, $t_{ion} + t_{elec} = 1$.

Thermal transport

Temperature-dependent thermal conductivity was measured on a Li_2SiAs_2 pellet of greater than 85% geometrical density in the temperature range of 2–300 K on a commercial multipurpose Physical Properties Measurement System (PPMS, Quantum Design) using the Thermal Transport Option.

Results/discussion

Both compounds can be synthesized using elements as precursors. The high Li content in Li_2SiAs_2 requires the use of

3324 | *J. Mater. Chem. A*, 2020, **8**, 3322–3332

This journal is © The Royal Society of Chemistry 2020

Nb crucibles to avoid Li losses through reactions with silica. This compound was synthesized as almost single-phase sample. In the case of $LiSi_3As_6$, samples with significant amounts of the target phase were produced, but single-phase samples were not achieved despite multiple efforts. $LiSi_3As_6$ appears very stable, demonstrating long term air stability, as well as stability in H_2O and 6 M HCl washes for at least 30 minutes. On the other hand, Li_2SiAs_2 is more air-sensitive, showing significant signs of degradation after a couple minutes of exposure to ambient conditions. This drastic disparity in stability may stem from the large difference in the Li contents. The decrease of the stability with the increase of the formal negative charge on the pnictide polyanion was observed in the Cs–Si–As system. For example, $Cs_{0.16}SiAs_2$ is water stable, while Cs_2SiAs_2 is moisture sensitive and Cs_5SiAs_3 is air sensitive.[30–32] Similarly, $Li_3Si_7As_8$ with a Li content between $LiSi_3As_6$ and Li_2SiAs_2 was reported to be mildly air-sensitive and moisture sensitive.[20]

Differential scanning calorimetry (DSC) was used to investigate the thermal stabilities of the title phases. DSC of $LiSi_3As_6$ exhibits two peaks upon heating, the first at 801 K is attributed to the sublimation of elemental arsenic impurities in the sample, while the peak at 995 K is the melting/decomposition of $LiSi_3As_6$; however no sharp peaks corresponding to recrystallization were observed upon cooling (Fig. S1† top). PXRD of the sample after the DSC measurement shows the major phase to be $SiAs_2$, with a Si impurity which was in the initial sample (Fig. S2†). DSC experiment indicates that upon heating a peritectic decomposition of $LiSi_3As_6$ into $SiAs_2$ took place. The DSC experiment was performed in a silica container and the released Li may have reacted with silica at high temperature. The melting point of $SiAs_2$ is 1250 K which is higher than the maximum temperature used in the DSC experiment. Thus, $SiAs_2$ was not melted and no sharp crystallization peaks were observed upon cooling. For Li_2SiAs_2, DSC shows the onset of melting at 1167 K with a sharp crystallization peak beginning at 740 K (Fig. S1†
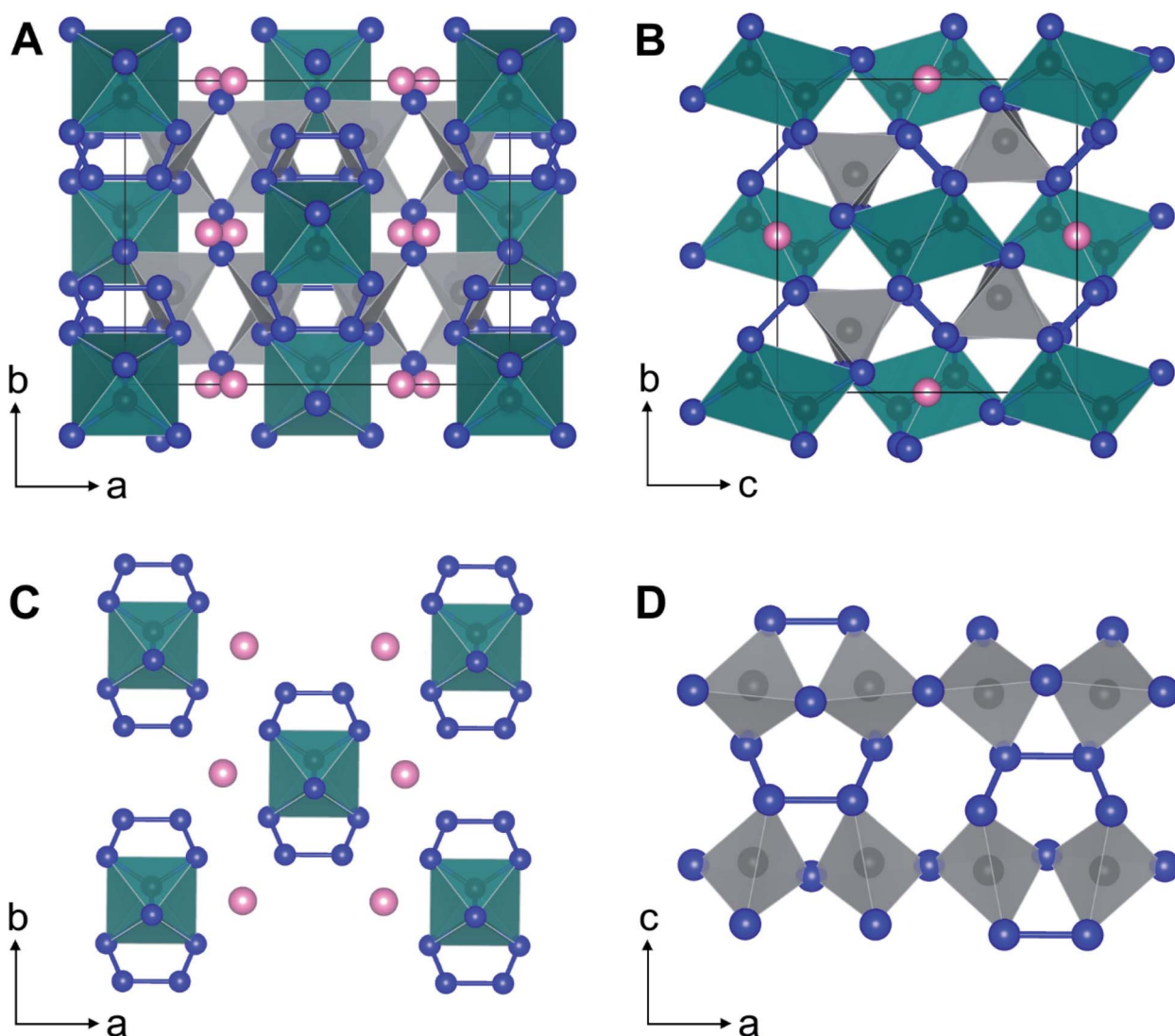

Fig. 3 Crystal structure of $LiSi_3As_6$. (A) and (B) general views along [001] and [100]; (C) view of the Si_2As_6 antiprism slab omitting the tetrahedra; (D) view of the $SiAs_4$ tetrahedral slab. Unit cell shown as black lines, Li: pink, Si: black, As: blue, $SiAs_4$: gray, Si_2As_6: teal.

bottom). The melting temperature was higher than the synthesis temperature of 923 K. PXRD of the products after the DSC measurement shows that the sample contains mainly Li_2SiAs_2 with SiAs impurities, most likely due to the Li reacting with the silica ampoule during heating.

LiSi$_3$As$_6$ crystallizes in the orthorhombic *Cmce* space group (No. 64), Pearson symbol *oS*-80. Similar to a number of complex ternary silicon phosphides,[33–40] LiSi$_3$As$_6$ exhibits several different bonding schemes including corner sharing SiAs$_4$ tetrahedra, Si–Si dumbbells, and As–As bonds. The structure is composed of alternating planes of SiAs$_4$ tetrahedra and Si$_2$As$_6$ antiprisms along the *b*-direction (Fig. 3A and B). The SiAs$_4$ tetrahedra have Si–As distances of 2.316(2)–2.405(2) Å, similar to distances reported in compounds such as Cs$_5$SiAs$_3$, Li$_3$Si$_7$As$_8$, and CeSiAs$_3$, among others.[20,32,41–47] These tetrahedra are interconnected through three different bonding arrangements to form a slab, shown in Fig. 3D. Along [100] direction, chains of corner sharing tetrahedra are further linked through

alternating As–As bonds which are 2.512(2) Å in length. These chains are combined into a slab by perpendicular As–As bonds of 2.445(1) Å along the [001] direction between neighboring chains (Fig. 3D). Both As–As distances are within reported lengths observed for As–As bonds.[41,42,48–51]

The plane of Si$_2$As$_6$ antiprisms is formed through isolated Si$_2$As$_6$ units, which are surrounded by 6 Li atoms in the *ab*-plane, shown in Fig. 3C. The Si–Si distance in these antiprisms is 2.341(6) Å, while the Si–As distances measure 2.367(2)–2.387(3) Å, all within typical reported distances taking into account covalent radii for Si (1.17 Å) and As (1.22 Å).[20,32,36,41–47,52–54,58] The Li atoms within this plane have distorted octahedral coordination with Li–As distances of 2.83(2)–2.95(2) Å, which fall within reported values.[19,20,55–57] All As atoms in the Si$_2$As$_6$ units are corner shared with SiAs$_4$ tetrahedra from neighboring slabs along the *b*-direction, creating the complex 3D structural arrangement.
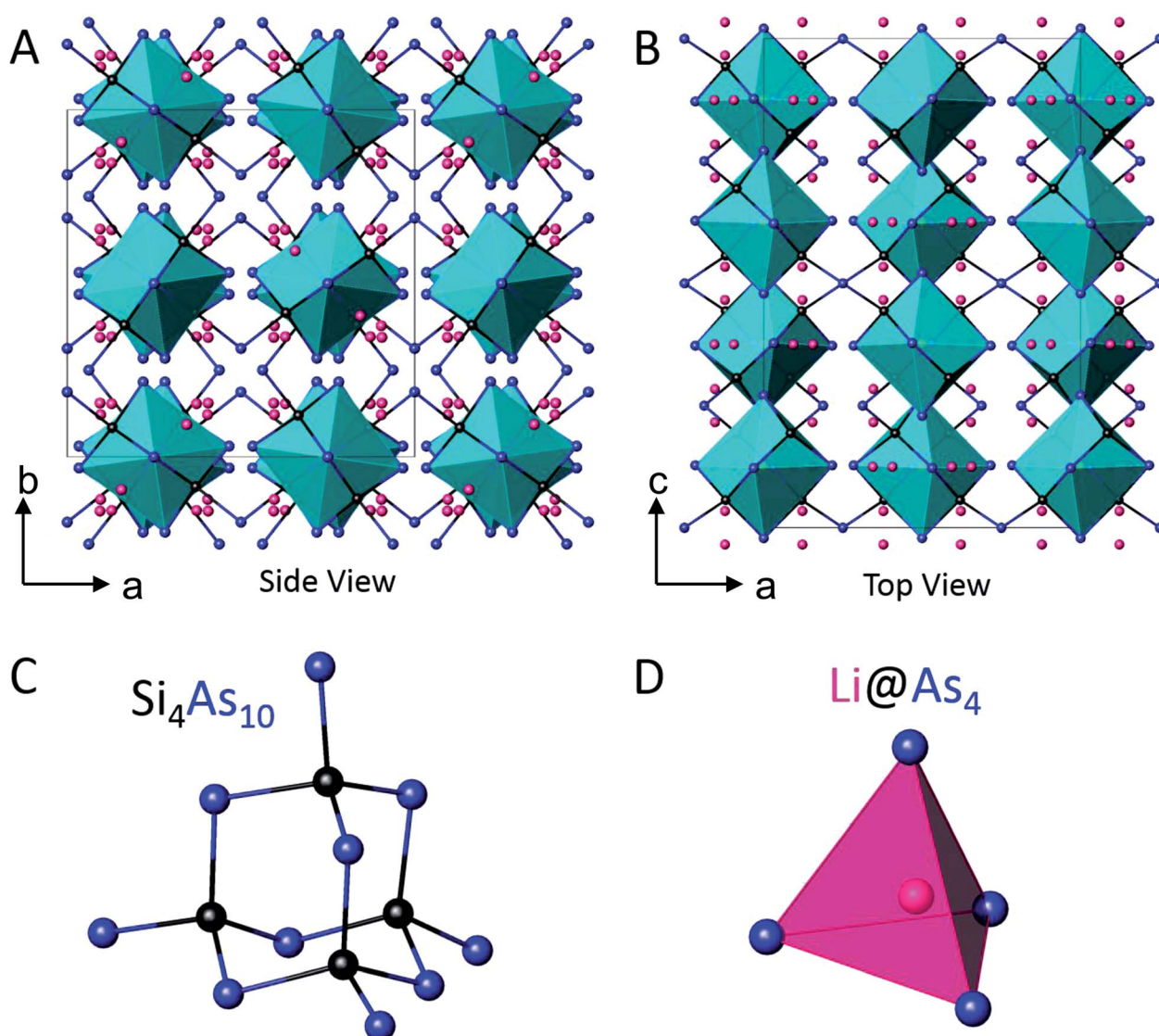

Fig. 4 Crystal structure of Li$_2$SiAs$_2$. (A) and (B) general views; (C) Si$_4$As$_{10}$ adamantane-like fragment; (D) Li coordination. Unit cell shown as black lines, Li: pink, Si: black, As: blue, Li@As$_4$: pink, Si$_4$As$_{10}$: teal.

3326 | *J. Mater. Chem. A*, 2020, **8**, 3322–3332

This journal is © The Royal Society of Chemistry 2020

$LiSi_3As_6$ has a Wyckoff sequence of g^3f^2ed. Other compounds with this Wyckoff sequence include Ta_6Br_{14}, Ta_6I_{14}, CuP_4Se_4I, and $MnTl_2As_2S_5$.[59–62] Ta_6Br_{14} and Ta_6I_{14} contain isolated clusters forming 1D structures, while CuP_4Se_4I crystallizes in a 2D layered structure.[59–61] Previously $MnTl_2As_2S_5$ was the only 3D phase reported with this Wyckoff sequence, however this structure lacks homoatomic bonds like the Si–Si bonds found in $LiSi_3As_6$.[62]

Li_2SiAs_2 crystallizes in the tetragonal space group $I4_1/acd$ (No. 142) in the same structure type as Na_2SnAs_2 and Li_2SiP_2.[17,18,63] Adamantane-like Si_4As_{10} units are connected to each other through shared As atoms (Fig. 4). In the structure, each Si atom is coordinated by four As atoms forming a tetrahedron while each

As is coordinated by two Si atoms (Fig. 4C). Li atoms are tetrahedrally coordinated by four As atoms (Fig. 4D). The Si–As bond distances found in Li_2SiAs_2 are in a much narrower range compared to $LiSi_3As_6$, falling between 2.3424(8)–2.3778(7) Å. These bond lengths fall in the mid-range of those found in $LiSi_3As_6$, matching common lengths in other compounds.[20,32,41–47] The Li–As distances range from 2.516(3)–2.853(1) Å and are shorter than those found in $LiSi_3As_6$, however they span distances found for other reported Li–As containing compounds and are not nearly as short as distances found in $Li_3Si_7As_8$.[19,20,55–57] Larger alkali metals, A = K, Rb, and Cs, form 2–1–2 compounds, A_2SiAs_2.[32,44,64] In the crystal structure of these compounds one-dimensional anionic $[SiAs_2]^{2-}$ chains composed of edge-sharing

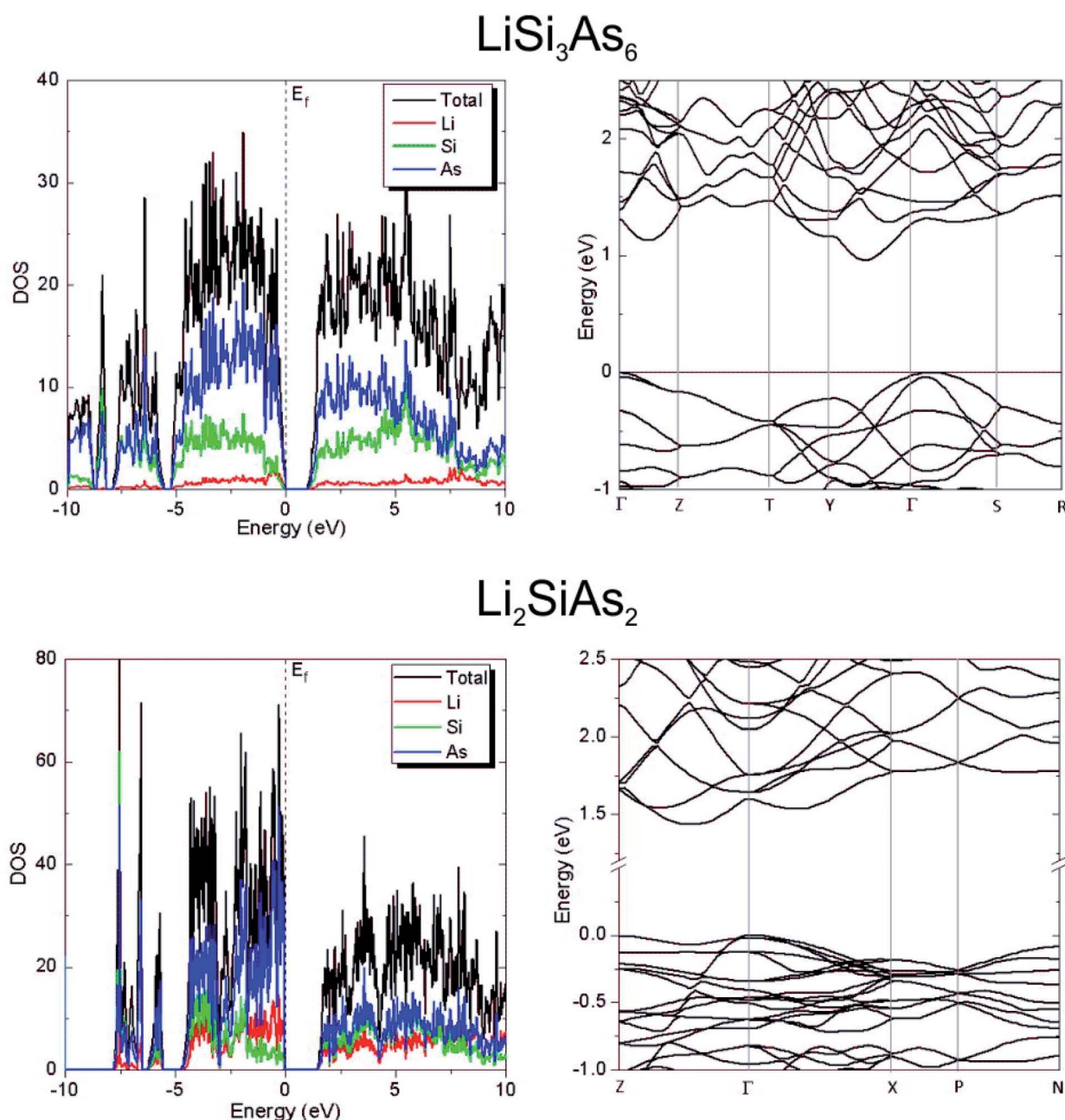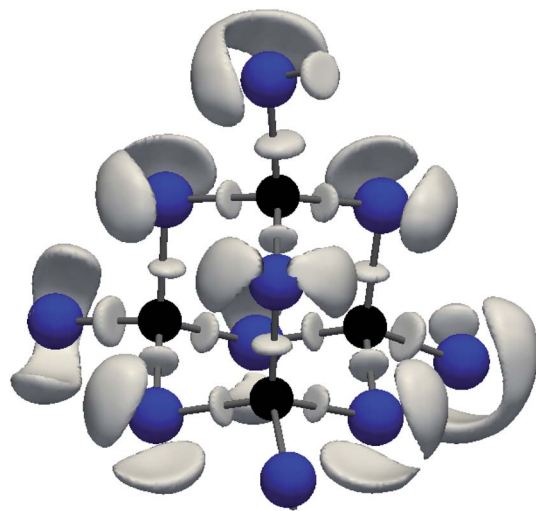Fig. 5   Density of states and band structures for $LiSi_3As_6$ (top) and Li_2SiAs_2 (bottom).

Fig. 6 Electron localization function isosurface ($\eta = 0.84$) for Li_2SiAs_2. Si: black, As: blue.

$SiAs_4$ tetrahedra are present. A reduction of the cation size leads to rearrangements of the same building units, $SiAs_4$ tetrahedra, into a three-dimensional framework.

We have previously shown that the parent $SiAs_2$ binary compound is able to accommodate ~0.16 cations as large as Cs per formula unit in the interlayer space forming $Cs_{0.16}SiAs_{2-x}$

without significant modification of the 2D $SiAs_2$ layers, given that the extra electrons are compensated either by As vacancy formation or by aliovalent M/Si substitutions (M = Ga, Zn, Cu).[30] Further increase of the cation content leads to the structural reconstruction in the Si–As framework. Doubling the cation content in the case of $LiSi_3As_6$ (=$Li_{0.33}SiAs_2$) results in a collapse of the layered structure of $SiAs_2$ into a 3D framework with the formation of Si–Si bonds. However, $LiSi_3As_6$ maintains the $SiAs_4$ corner-sharing and As–As bonding within a "layer," similar to the Si–As layers found in $SiAs_2$.[42] The Li_2SiAs_2 stoichiometry results in more drastic structural rearrangements due to the excess electrons added to the Si–As network. This results in the removal of homoatomic bonds, as the Li_2SiAs_2 no longer contains any Si–Si or As–As bonds. Partial removal of homoatomic bonds was also observed for the Li incorporation into SiAs to form $Li_3Si_7As_8$.[20]

Considering a polar bonding scheme for $LiSi_3As_6$, each tetrahedral Si can be considered as Si^{4+}, while each Si in the antiprism can be considered as Si^{3+}. Similarly, As coordinated to three or two Si atoms is As^{3-}, while As atoms forming one or two bonds to As atoms are As^{2-} and As^-, respectively. This bonding scheme results in the electron balanced composition of $(Li^+)(Si^{4+})_2(Si^{3+})(As^{3-})_2(As^{2-})_2(As^-)_2$. Alternatively, the Si–As bonds can be considered as covalent bonds where the electron pair is shared between As and Si. In such a description four-coordinated Si atoms and three-coordinated As atoms have
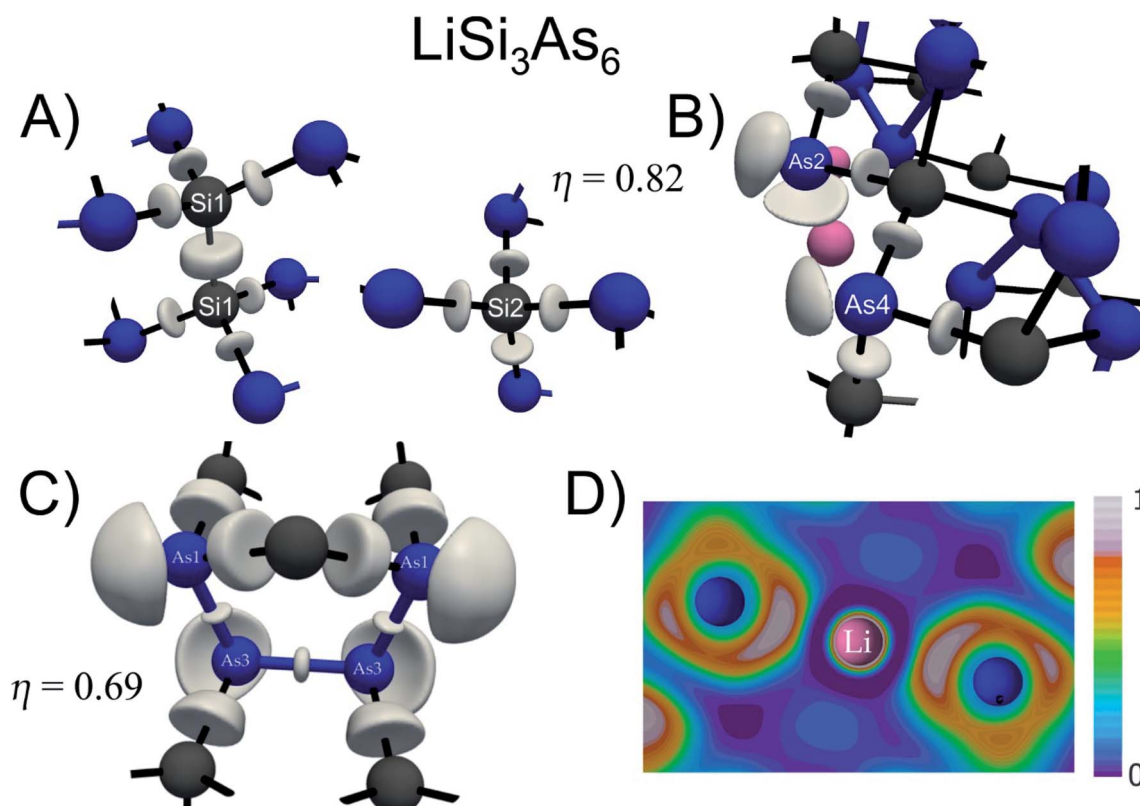

Fig. 7 Chemical bonding in $LiSi_3As_6$ according to electron localization function (ELF, η) analysis: 3D isosurfaces of ELF showing bonding around (A) Si atoms, $\eta = 0.82$; (B) As2 and As4 atoms, $\eta = 0.82$; (C) As1–As3–As3–As1 fragment, $\eta = 0.69$; (D) coloring of the ELF distributions for a slice of the crystal structure of $LiSi_3As_6$ containing Li atom. As: blue; Si; black, Li: pink.

3328 | *J. Mater. Chem. A*, 2020, **8**, 3322–3332

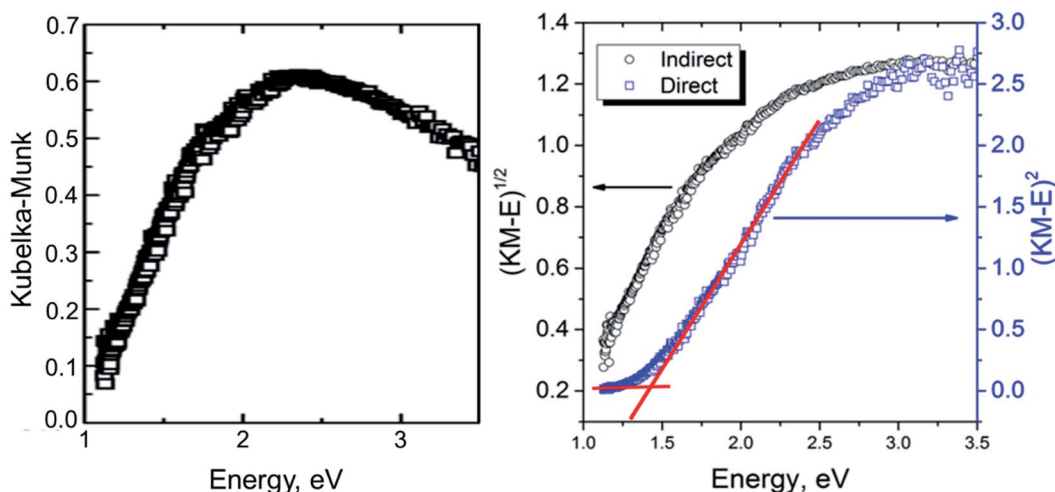This journal is © The Royal Society of Chemistry 2020

Fig. 8 Solid-state UV-vis Kubelka–Munk diffuse reflectance spectrum of Li_2SiAs_2 (left). Tauc plots for allowed direct and indirect transitions (right).

oxidation states of 0, while two-coordinated As atoms have formal oxidation states of −1, leading to the electron-balanced formula $(Li^+)(Si^0)_3(As^0)_5(As^-)$. For Li_2SiAs_2, both polar and covalent assignments of the oxidation states result in charge balanced compositions of $(Li^+)_2(Si^{4+})(As^{3-})_2$ and $(Li^+)_2(Si^0)(As^-)_2$, respectively.

To gain a better understanding of the bonding in these phases electronic structure calculations were performed using the TB-LMTO-ASA program.[22] From the band structures and DOS, $LiSi_3As_6$ and Li_2SiAs_2 were found to be indirect semiconductors with bandgaps of 0.97 eV and 1.43 eV, respectively (Fig. 5). For Li_2SiAs_2 both direct transitions at the Z and Γ points have larger energy of 1.67 eV, while for $LiSi_3As_6$ the direct transition at the Γ point is 1.31 eV. The density of states for both phases exhibit significant contributions from Si and As in the conduction and valence bands, suggesting strong covalent bonding in the Si–As frameworks. For Li_2SiAs_2 electron localization function analysis shows the expected covalent bonding between Si and As with two electron lone pairs on each As atom (Fig. 6). This is expected because each As is coordinated to two silicon atoms. This result favors the covalent description of the chemical bonding in Li_2SiAs_2 as $(Li^+)_2(Si^0)(As^-)_2$.

Analysis of the chemical bonding in $LiSi_3As_6$ also supports the covalent nature of the Si–As interactions. Si1 atoms are engaged in the three covalent Si–As bonds in addition to the Si1–Si1 covalent bond, while Si2 atoms form four Si–As bonds similar to Si atoms in Li_2SiAs_2 (Fig. 7A). As4 forms three As–Si bonds and has an electron lone pair (Fig. 7B). Every As atom in the $SiAs_4$ pentagonal ring fragment has one electron lone pair in addition to two As–Si + one As–As bonds (for As1) or two As–As + one As–Si bonds (for As3) (Fig. 7C). Finally, two coordinated As2 is an analogue of the As atoms in Li_2SiAs_2, possessing two-electron lone pairs in addition to two As–Si bonds, which supports its description as As^- (Fig. 7B). Li atoms are not engaged in the covalent bonding and have spherical distribution of ELF corresponding to core 2s electrons (Fig. 7D).

To confirm the theoretical bandgap of Li_2SiAs_2 diffuse reflectance spectroscopy was utilized to determine the experimental bandgap. Measurements were performed on pellets sealed under argon inside polypropylene bags to prevent sample oxidation during data collection. Tauc plots of Li_2SiAs_2 show that it has an indirect transition of less than the instrument limit of 1.1 eV and a direct transition of 1.40 eV (Fig. 8). The large bandgaps are supported by quantum chemical calculations and by the red-brown color of the crystals. Due to the black color of $LiSi_3As_6$ and Si impurities in samples the experimental band gap was not measured for $LiSi_3As_6$.

Presence of significant amounts of Si and As impurities in the samples of $LiSi_3As_6$ prevented property characterization for this silicon-arsenide. However, Li_2SiAs_2 was synthesized near single-phase and its thermal, charge, and ion conductivities
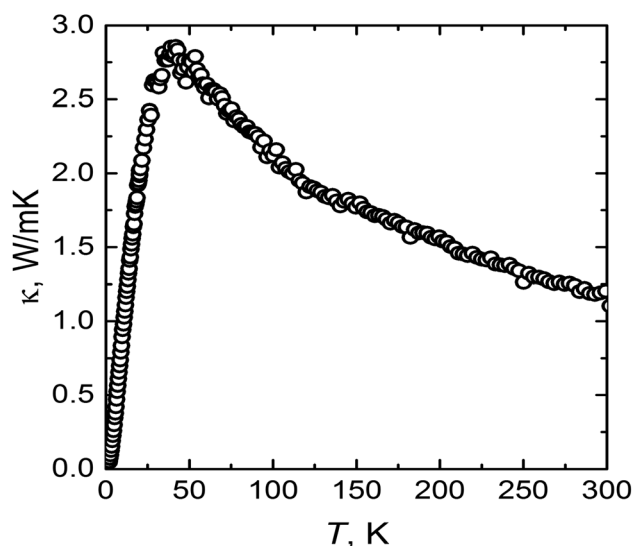

Fig. 9 Temperature-dependent thermal conductivity of Li_2SiAs_2.

This journal is © The Royal Society of Chemistry 2020

J. Mater. Chem. A, 2020, **8**, 3322–3332 | **3329**

were studied in detail. Li_2SiAs_2 is expected to have a low thermal conductivity due to the large number of atoms in the unit cell and overall complexity of the crystal structure which should result in complex phonon structure. The measured temperature-dependent thermal conductivity has a typical trend for crystalline compounds with a peak at 50 K and decreasing thermal conductivity as a function of increasing temperature at higher temperatures due to Umklapp phonon–phonon scattering (Fig. 9). At 300 K the thermal conductivity reaches a value of 1.20 W m^{-1} K^{-1}. The electrical resistivity of Li_2SiAs_2 was too high to be measured using the Physical Property Measurement System. We estimated the electrical resistivity to be above 10 kΩ m at room temperature based on our previous experience with highly resistive compounds and PPMS.[65,66] The impedance measurements confirmed high dc electrical resistivity of the Li_2SiAs_2 to be over 70 kΩ m.

Given the isostructural nature of Li_2SiAs_2 to Li_2SiP_2 and the promising Li-ion conductivity observed in the latter,[17,18] the Li-conductivity of a pressed pellet of Li_2SiAs_2 was characterized. Fig. 10 shows the temperature-dependence of the bulk electrical conductivity for Li_2SiAs_2 with a room temperature conductivity of 7×10^{-6} S cm^{-1}. The impedance curves are provided in the Fig. S4 and S5.† This conductivity is over an order of magnitude greater than that of the analogous phosphide (4×10^{-7} S cm^{-1}) and nitride (8×10^{-8} S cm^{-1}) phases,[17,67] indicating the potential of Li_2SiAs_2 as a solid-state Li-ion conductor. This conductivity may be further enhanced through trivalent doping, as predicted for Li_2SiP_2 by Yeandel et al.[68] or even by increasing the Li content as seen by enhanced performance when going from Li_8SiP_4 to the related $Li_{14}SiP_6$.[15] The activation energy for conduction is calculated from the slope of conductivity using an Arrhenius expression of $\sigma(T) = \sigma_0 \exp(-E_a/kT)$ and found to be $E_a = 0.53$ eV. DC polarization experiments reveal the ionic transference number is 0.98, indicating the conductivity is almost entirely ionic in character, which is a prerequisite for solid ionic conductor applications in Li-ion batteries. A combination of high Li-ionic conductivity with low electrical conductivity suggests Li_2SiAs_2 is a promising solid-state Li-ion conductor.

Conclusions

Two new phases in the Li–Si–As ternary system have been synthesized and characterized. $LiSi_3As_6$ crystallizes in a new structure type and its structural complexity demonstrates that the various bonding schemes often observed in tetrel-phosphides can also be displayed in the less studied tetrel-arsenides. Li_2SiAs_2 is isostructural to previously reported Li_2SiP_2 and exhibits ionic conductivity that is an order of magnitude greater than that of the phosphide and nitride analogues, in line with the increase of size and decrease in electronegativity of As compared to P and N. These two new phases add to the recently growing Li–Si–As phase space and indicate there is much to be explored in this system in terms of phase identification and property characterization.

Conflicts of interest

There are no conflicts to declare.

Acknowledgements

References

1 P. Knauth, *Solid State Ionics*, 2009, **180**, 911–916.

2 Y. Meesala, A. Jena, H. Chang and R.-S. Liu, *ACS Energy Lett.*, 2017, **2**, 2734–2751.

3 S.-C. Li, J.-Y. Cai and Z.-X. Lin, *Solid State Ionics*, 1988, **28–30**, 1265–1270.

4 Y. Deng, C. Eames, B. Fleutot, R. David, J. N. Chotard, E. Suard, C. Masquelier and M. S. Islam, *ACS Appl. Mater. Interfaces*, 2017, **9**, 7050–7058.

5 S. Narayanan, F. Ramezanipour and V. Thangadurai, *J. Phys. Chem. C*, 2012, **116**, 20154–20162.

6 A. Bhandari and J. Bhattacharya, *J. Phys. Chem. C*, 2016, **120**, 29002–29010.

7 N. Kamaya, K. Homma, Y. Yamakawa, M. Hirayama, R. Kanno, M. Yonemura, T. Kamiyama, Y. Kato, S. Hama, K. Kawamoto and A. Mitsui, *Nat. Mater.*, 2011, **10**, 682–686.

8 A. Kuhn, J. Kohler and B. V. Lotsch, *Phys. Chem. Chem. Phys.*, 2013, **15**, 11620–11622.

9 P. Bron, S. Johansson, K. Zick, J. Schmedt auf der Gunne, S. Dehnen and B. Roling, *J. Am. Chem. Soc.*, 2013, **135**, 15694–15697.
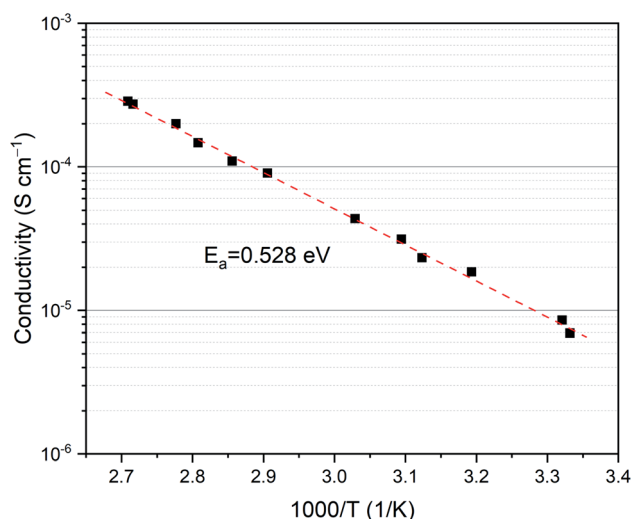

Fig. 10 Arrhenius plot of the ionic conductivity temperature dependence for Li_2SiAs_2.

3330 | *J. Mater. Chem. A*, 2020, **8**, 3322–3332

This journal is © The Royal Society of Chemistry 2020

10 A. Kuhn, O. Gerbig, C. Zhu, F. Falkenberg, J. Maier and B. V. Lotsch, *Phys. Chem. Chem. Phys.*, 2014, **16**, 14669–14674.

11 Y. Kato, R. Saito, M. Sakano, A. Mitsui, M. Hirayama and R. Kanno, *J. Power Sources*, 2014, **271**, 60–64.

12 S. P. Ong, Y. Mo, W. D. Richards, L. Miara, H. S. Lee and G. Ceder, *Energy Environ. Sci.*, 2013, **6**, 148–156.

13 I. Tarhouchi, V. Viallet, P. Vinatier and M. Ménétrier, *Solid State Ionics*, 2016, **296**, 18–25.

14 P. G. Bruce, B. Scrosati and J. M. Tarascon, *Angew. Chem., Int. Ed.*, 2008, **47**, 2930–2946.

15 S. Strangmuller, H. Eickhoff, D. Muller, W. Klein, G. Raudaschl-Sieber, H. Kirchhain, C. Sedlmeier, V. Baran, A. Senyshyn, V. L. Deringer, L. van Wullen, H. A. Gasteiger and T. F. Fässler, *J. Am. Chem. Soc.*, 2019, **141**, 14200–14209.

16 H. Eickhoff, L. Toffoletti, W. Klein, G. Raudaschl-Sieber and T. F. Fässler, *Inorg. Chem.*, 2017, **56**, 6688–6694.

17 L. Toffoletti, H. Kirchhain, J. Landesfeind, W. Klein, L. van Wullen, H. A. Gasteiger and T. F. Fässler, *Chem.–Eur. J.*, 2016, **22**, 17635–17645.

18 A. Haffner, T. Bräuniger and D. Johrendt, *Angew. Chem., Int. Ed.*, 2016, **55**, 13585–13588.

19 R. Juza and W. Schulz, *Z. Anorg. Allg. Chem.*, 1954, **275**, 65–78.

20 J. Mark, M. P. Hanrahan, K. E. Woo, S. Lee, A. J. Rossini and K. Kovnir, *Chem.–Eur. J.*, 2019, **25**, 6392–6401.

21 G. M. Sheldrick, *Acta Crystallogr., Sect. A: Found. Crystallogr.*, 2008, **64**, 112–122.

22 O. Jepsen, A. Burkhardt and O. K. Andersen, *The Program TB-LMTO-ASA, Version 4.7*, Max-Planck-Institut fur Festkorperforschung, Stuttgart, Germany, 1999.

23 U. von Barth and L. Hedin, *J. Phys. C: Solid State Phys.*, 1972, **5**, 1629–1642.

24 A. D. Becke and K. E. Edgecombe, *J. Chem. Phys.*, 1990, **92**, 5397.

25 A. Savin, O. Jepsen, J. Flad, O. K. Andersen, H. Preuss and H. G. von Schnering, *Angew. Chem., Int. Ed. Engl.*, 1992, **31**, 187–188.

26 A. Savin, R. Nesper, S. Wengert and T. F. Fässler, *Angew. Chem., Int. Ed. Engl.*, 1997, **36**, 1808–1832.

27 Y. Grin, A. Savin and B. Silvi, in *The Chemical Bond: Fundamental Aspects of Chemical Bonding*, ed. G. Frenking and S. Shaik, Wiley-VCH, Weinheim, 2014, vol. 10, pp. 345–382.

28 Sandia National Labs, *Kitware Inc, Los Alamos National Labs, Paraview: Parallel visualization application, version 4.1.0 64-bit*, USA, http://paraview.org.

29 A. I. Baranov, *Visualization plugin for ParaView*, 2012.

30 K. E. Woo, J. A. Dolyniuk and K. Kovnir, *Inorg. Chem.*, 2019, **58**, 4997–5005.

31 B. Eisenmann and J. Klein, *J. Less-Common Met.*, 1991, **175**, 109–117.

32 B. Eisenmann, J. Klein and M. Somer, *Angew. Chem., Int. Ed. Engl.*, 1990, **29**, 87–88.

33 A. Haffner and D. Johrendt, *Z. Anorg. Allg. Chem.*, 2017, **643**, 1717–1720.

34 J. Mark, J.-A. Dolyniuk, N. Tran and K. Kovnir, *Z. Anorg. Allg. Chem.*, 2019, **645**, 242–247.

35 J. Mark, J. Wang, K. Wu, J. G. Lo, S. Lee and K. Kovnir, *J. Am. Chem. Soc.*, 2019, **141**, 11976–11983.

36 X. Zhang, T. Yu, C. Li, S. Wang and X. Tao, *Z. Anorg. Allg. Chem.*, 2015, **641**, 1545–1549.

37 S. Ono, H. Hayakawa and K. Nomura, *Nippon Kagaku Kaishi*, 1976, **11**, 1700–1709.

38 P. Kaiser and W. Jeitschko, *J. Solid State Chem.*, 1996, **124**, 346–352.

39 P. Kaiser and W. Jeitschko, *Z. Anorg. Allg. Chem.*, 1996, **622**, 53–56.

40 H. G. V. Schnering and G. Menge, *J. Solid State Chem.*, 1979, **28**, 13–19.

41 H. Hayakawa and S. Ono, *J. Less-Common Met.*, 1988, **144**, 177–194.

42 T. Wadsten, *Acta Chem. Scand.*, 1967, **21**, 593–594.

43 T. Wadsten, *Acta Chem. Scand.*, 1965, **19**, 1232–1238.

44 J. Wolf, D. Weber and H.-G. V. Schnering, *Z. Naturforschung B*, 1986, **41**, 731–735.

45 W. M. Hurng, J. D. Corbett, S. L. Wang and R. A. Jacobson, *Inorg. Chem.*, 1987, **26**, 2392–2395.

46 B. Eisenmann and H. Schäfer, *Angew. Chem., Int. Ed. Engl.*, 1980, **19**, 490–491.

47 K. E. Woo, J. Wang, K. Wu, K. Lee, J.-A. Dolyniuk, S. Pan and K. Kovnir, *Adv. Funct. Mater.*, 2018, **28**, 1801589.

48 K. A. Kovnir, A. V. Sobolev, I. A. Presniakov, O. I. Lebedev, G. V. Tendeloo, W. Schnelle, Y. Grin and A. V. Shevelkov, *Inorg. Chem.*, 2005, **44**, 8786–8793.

49 K. Ayouz, M. Kars, A. Rebbah and H. Rebbah, *Acta Crystallogr., Sect. E: Struct. Rep. Online*, 2009, **65**, i15.

50 J. V. Zaikina, K. A. Kovnir, A. V. Sobolev, I. A. Presniakov, Y. Prots, M. Baitinger, W. Schnelle, A. V. Olenev, O. I. Lebedev, G. Van Tendeloo, Y. Grin and A. V. Shevelkov, *Chem.–Eur. J.*, 2007, **13**, 5090–5099.

51 B. Saparov and A. S. Sefat, *J. Solid State Chem.*, 2012, **191**, 213–219.

52 T. Wadsten, *Chem. Scr.*, 1975, **8**, 63–69.

53 J. V. Zaikina, K. A. Kovnir, F. Haarmann, W. Schnelle, U. Burkhardt, H. Borrmann, U. Schwarz, Y. Grin and A. V. Shevelkov, *Chem.–Eur. J.*, 2008, **14**, 5414–5422.

54 J. V. Zaikina, K. A. Kovnir, U. Burkhardt, W. Schnelle, F. Haarmann, U. Schwarz, Y. Grin and A. V. Shevelkov, *Inorg. Chem.*, 2009, **48**, 3720–3730.

55 G. Brauer and E. Zintl, *Z. Phys. Chem. B*, 1937, **37**, 323–352.

56 D. T. Cromer, *Acta Crystallogr.*, 1959, **12**, 36–41.

57 K. Lee, D. Kaseman, S. Sen, I. Hung, Z. Gan, B. Gerke, R. Pottgen, M. Feygenson, J. Neuefeind, O. I. Lebedev and K. Kovnir, *J. Am. Chem. Soc.*, 2015, **137**, 3622–3630.

58 W. Hönle, J. Buresch, K. Peters, J. H. Chang and H. G. von Schnering, *Z. Kristallogr. - New Cryst. Struct.*, 2002, **217**, 485–486.

59 B. Bajan and H.-J. Meyer, *Z. Kristallogr. - Cryst. Mater.*, 1995, **210**, 607.

60 H. M. Artelt and G. Meyer, *Z. Kristallogr. - Cryst. Mater.*, 1993, **206**, 306–307.

This journal is © The Royal Society of Chemistry 2020

J. Mater. Chem. A, 2020, **8**, 3322–3332 | **3331**

61 A. Pfitzner, S. Reiser and H.-J. Deiseroth, *Z. Anorg. Allg. Chem.*, 1999, **625**, 2196–2201.

62 M. Gostojić, A. Edenharter, W. Nowacki and P. Engel, *Z. Kristallogr. - Cryst. Mater.*, 1982, **158**, 43–52.

63 M. Asbrand and B. Eisenmann, *Z. Naturforschung B*, 1993, **48**, 452–456.

64 W.-M. Hurng, E. S. Peterson and J. D. Corbett, *Inorg. Chem.*, 1989, **28**, 4177–4180.

65 J. Wang, K. Lee and K. Kovnir, *J. Mater. Chem. C*, 2015, **3**, 9811–9818.

66 J. Wang, J. T. Greenfield and K. Kovnir, *J. Solid State Chem.*, 2016, **242**, 22–27.

67 H. Yamane, S. Kikkawa and M. Koizumi, *Solid State Ionics*, 1987, **25**, 183–191.

68 S. R. Yeandel, D. O. Scanlon and P. Goddard, *J. Mater. Chem. A*, 2019, **7**, 3953–3961.

3332 | *J. Mater. Chem. A*, 2020, **8**, 3322–3332

This journal is © The Royal Society of Chemistry 2020